The Astrophysical Journal, 590:917–931, 2003 June 20
© 2003. The American Astronomical Society. All rights reserved. Printed in U.S.A.

TRAPPED PROTOSTELLAR WINDS AND THEIR BREAKOUT

Francis P. Wilkin
Instituto de Astronomía, Universidad Nacional Autónoma de México, Apdo Postal 70-264, 58089 Morelia, México;
f.wilkin@astrosmo.unam.mx

and

Steven W. Stahler
Department of Astronomy, University of California, 601 Campbell Hall, Berkeley, CA 94720-3411;
stahler@astron.berkeley.edu
Received 2002 December 20; accepted 2003 March 3

ABSTRACT

Observations show that high-velocity jets stem from deeply embedded young stars, which may still be experiencing infall from their parent cloud cores. Yet theory predicts that, early in this buildup, any outgoing wind is trapped by incoming material of low angular momentum. As collapse continues and brings in more rapidly rotating gas, the wind can eventually break out. Here we model this transition by following the motion of the shocked shell created by impact of the wind and a rotating, collapsing envelope. We first demonstrate, both analytically and numerically, that our previous, quasi-static solutions are dynamically unstable. Our present, fully time-dependent calculations include cases both where the wind is driven back by infall to the stellar surface and where it erupts as a true outflow. For the latter, we find that the time of breakout is 5×10^4 yr for wind speeds of 200 km s^{-1}. The reason for the delay is that the shocked material, including the swept-up infall, must be able to climb out of the star's gravitational potential well. We explore the critical wind speed necessary for breakout as a function of the mass transport rates in the wind and infall, as well as the cloud rotation rate Ω_0 and time since the start of infall. Breakout does occur for realistic parameter choices. The actual breakout times would change if we relaxed the assumption of perfect mixing between the wind and infall material. Our expanding shells do not exhibit the collimation of observed jets but continue to expand laterally. To halt this expansion, the density in the envelope must fall off less steeply than in our model.

Subject headings: circumstellar matter — hydrodynamics — ISM: jets and outflows — shock waves — stars: mass loss — stars: pre–main-sequence

1. INTRODUCTION

The traditional picture of low-mass star formation in isolation (Shu, Adams, & Lizano 1987) envisions an early period of pure accretion, prior to the appearance of any wind. This expectation is based on simple theoretical considerations. Since the star is building up mass from its parent cloud, the rate of mass infall exceeds that of any outflow. In addition, both theory and observation suggest that the *speeds* of infalling and wind gas are comparable. Thus, the ram pressure from the collapsing envelope should crush the wind, preventing its escape from the stellar or inner disk surface. Why is it, then, that the most embedded stars, including those designated Class 0 (André, Ward-Thompson, & Barsony 1993), are observed to produce vigorous winds? How do wind and infall simultaneously occur in a very young object?

The answer, as has long been appreciated, is that neither flow is isotropic. Rotation and magnetic fields, in both the star and cloud, break spherical symmetry and alter the geometry of the wind and infall. Moreover, rotational distortion increases as the collapse of the parent cloud proceeds in an inside-out fashion (Shu 1977). Our goal in this paper is to examine numerically the interaction between wind and infall. Since the full situation is complex, it is best to proceed in stepwise fashion. We concentrate, therefore, on the effect of infall geometry, positing for simplicity a spherical wind. We also focus exclusively on the rotational influence. That is, we neglect any magnetic force on the infalling gas, under the assumption that decoupling from the ambient field has already occurred (Li & McKee 1996).

As in our first study of this topic (Wilkin & Stahler 1998, hereafter Paper I), we follow the dynamics of the thin shell formed by the colliding wind and infall. Paper I derived an evolutionary sequence of shells under the simplifying assumption of quasi-steady flow. That is, we took the expansion or contraction of the shell to be slow compared to either the wind or infall speeds. We now study the matter in more detail, solving the initial value problem of shell motion in a fully time-dependent manner. Our finding, in brief, is that the shell can either break out or recollapse to the star, depending on both the flow parameters and the epoch during cloud collapse. We derive the time of breakout as a function of the wind and infall parameters and explain how to generalize this to the case of an anisotropic driving wind.

In § 2 we first detail the mathematical formulation of the problem, obtaining the time-dependent version of the dynamical equations. After describing our method of solution in § 3, we show in § 4 that our previous, quasi-steady shells are in fact dynamically unstable. We set up our initial conditions and nondimensionalization of the launch problem in § 5, before presenting an overview of our numerical results in § 6. We also rederive key findings in a heuristic, analytical fashion. Finally, § 7 discusses the broader astrophysical implications of our study. In particular, an observational signature of the trapped wind phase may be fluctuations of the accretion luminosity, as an oscillatory

shock structure is expected to develop prior to breakout of the wind.

2. FORMULATION OF THE PROBLEM

2.1. *Thin-Shell Approximation*

The supersonic collision of wind and infall leads to the formation of both an inner and outer shock front. At the wind speeds appropriate for low-mass stars (typically less than 300 km s^{-1}), the cooling behind these shocks is relatively efficient (recall the discussion in § 2.2 of Paper I). Hence, we may describe the intershock region as a cold, thin shell, characterized by its radius $R(\theta, t)$ and mass surface density $\sigma(\theta, t)$. Here θ is the polar angle measured from the rotation axis of the parent cloud. As in Paper I, we assume this shell to be axisymmetric, i.e., invariant with respect to the azimuthal angle ϕ.

Within the shell, two fluids with very different temperature and velocity come into contact. The internal shearing layers are subject to the Kelvin-Helmholtz instability, which leads quickly to turbulent mixing. We shall assume that the mixing is so efficient that we may describe the shell as a single fluid with a time-averaged velocity at each point (R, θ, t). This velocity has an azimuthal component arising from rotation of the infalling envelope. It also has a meridional component along the shell. Furthermore, we do *not* neglect, as in Paper I, the velocity of the shell normal to the surface.

The evolution of the shell is governed by the incident fluxes of mass and momentum from the wind and infall. It is also influenced critically by the gravitational attraction of the star for the shell material. The central difference of the present study and Paper I is that we no longer assume the evolution to be quasi-steady; that is, the properties of the shell are allowed to change over the time required for material to travel along the surface.

2.2. *Description of Infall and Outflow*

The infall arises from the gravitational collapse of a dense cloud core within a larger molecular cloud. To obtain the resulting accretion flow, we idealize this core as a singular isothermal sphere rotating rigidly with angular velocity Ω_0. Our calculation does not address the formation of the core itself and neglects any turbulence in the initial structure. Recent theoretical work (e.g., Cho, Lazarian, & Vishniac 2002; Vazquez-Semadeni, Ballesteros-Paredes, & Klessen 2003) suggests how cores might condense out of a turbulent flow. Nevertheless, observations continue to show that nonthermal motion in the core itself is relatively small (Barranco & Goodman 1998). Once the infalling gas becomes supersonic, the effects of this turbulent component are expected to be minor. Our adoption of a spherical body, while clearly an idealization, should be of little consequence for the flow deep within the core's center.

In any event, the distributions of infalling density ρ_i and velocity $\boldsymbol{u}_i$ depend on time because the collapsing region spreads out as a rarefaction wave at the isothermal sound speed a_0, gradually engulfing material of higher specific angular momentum (Shu 1977). We adopt the infall model of Cassen & Moosman (1981), which represents the inner limit of the full collapse. This limit applies to radii that are small compared to the expansion front $R_{\rm exp} = a_0 t$, where t is the time since the collapse began.

We may gauge the total rate of infall by examining the transport of mass across a surface located well inside the expansion front. According to the inside-out collapse model of Shu (1977), this transport rate is

$$\dot{M}_i = \frac{m_0 a_0^3}{G} , \tag{1}$$

where $m_0 = 0.975$. The infall itself is characterized by a time-dependent length scale, the centrifugal radius $R_{\rm cen}$. This is given by

$$R_{\rm cen} = \frac{1}{16} m_0^3 a_0 \Omega_0^2 t^3 ,$$
$$R_{\rm cen}({\rm AU}) = \frac{a_0}{0.2 \text{ km s}^{-1}} \left(\frac{\Omega_0}{2 \times 10^{-14} \text{ s}^{-1}} \right)^2 \left(\frac{t}{10^5 \text{ yr}} \right)^3 . \tag{2}$$

Our reference value for Ω_0 is chosen to be consistent with inferred rotation rates based on velocity gradients in cloud cores lacking embedded *IRAS* sources (Jijina, Myers, & Adams 1999). For an equator-on rotating core, this corresponds to a velocity gradient of 0.6 km s^{-1} pc^{-1}. In regions where $r \lesssim R_{\rm cen}$, rotational distortion of the flow is significant, and some of the infalling matter strikes the equatorial plane ($\theta = \pi/2$), forming a circumstellar disk. When $r \gg R_{\rm cen}$, the infall is nearly spherically symmetric. Equation (1) gives the *sum* of the mass per unit time impacting the star directly and that entering the disk.

In terms of the nondimensional radial variable $\zeta \equiv R_{\rm cen}/r$, the infall velocity components and density are (Terebey, Shu, & Cassen 1984)

$$u_{i,r} = -\left(\frac{GM_*}{r} \right)^{1/2} \left(1 + \frac{\cos\theta}{\cos\theta_0} \right)^{1/2} , \tag{3}$$

$$u_{i,\theta} = \left(\frac{GM_*}{r} \right)^{1/2} \left(\frac{\cos\theta_0 - \cos\theta}{\sin\theta} \right) \left(1 + \frac{\cos\theta}{\cos\theta_0} \right)^{1/2} , \tag{4}$$

$$u_{i,\phi} = \left(\frac{GM_*}{r} \right)^{1/2} \frac{\sin\theta_0}{\sin\theta} \left(1 - \frac{\cos\theta}{\cos\theta_0} \right)^{1/2} , \tag{5}$$

$$\rho_i = -\frac{\dot{M}_i}{4\pi r^2 u_{i,r}} [1 + 2\zeta P_2(\cos\theta_0)]^{-1} . \tag{6}$$

The function $P_2(\cos\theta_0)$ is the Legendre polynomial, where θ_0 is a Lagrangian variable that labels the streamlines. Specifically, θ_0 is the initial polar angle of each fluid element, just before it is overtaken by the rarefaction wave. This angle is given implicitly in terms of the instantaneous coordinates ζ and θ by the trajectory equation

$$\zeta = \frac{\cos\theta_0 - \cos\theta}{\sin^2\theta_0 \cos\theta_0} . \tag{7}$$

Our goal is to assess the collimating influence of the anisotropic infall. Accordingly, we idealize the wind to be spherically symmetric, with an associated mass transport rate of $\dot{M}_w$. If the star lies at the origin of a spherical coordinate system, then the wind density at a radial distance r is

$$\rho_w = \frac{\dot{M}_w}{4\pi r^2 V_w} . \tag{8}$$

Here $V_w \equiv u_{w,r}$ is the wind velocity. Note that the components $u_{w,\theta}$ and $u_{w,\phi}$ are both zero.

We do not investigate the structure of the star, which is taken simply to be a spherical, gravitating mass. The value

of this mass is

$$M_* = \dot{M}_i t \ . \tag{9}$$

Thus, we assume that both the matter entering the disk and that colliding with the infall are efficiently recycled to the star. How gas within the shocked shell reaches the disk is, of course, one of our main concerns. On the other hand, the transport of matter *within* the disk through internal torques is beyond the scope of this project. Once the shell truly moves dynamically, mass accretion onto the star and disk is halted, and we freeze the stellar mass at the value corresponding to the launch time of the shell (see § 4).

2.3. *Time-dependent Equations: Mathematical Derivation*

As in Paper I, we consider a small, three-dimensional patch of the shell, whose center is located at (R, θ, ϕ) within a global, spherical coordinate system centered on the star. We also utilize a global, Cartesian system (x, y, z) (see Fig. 3 of Paper I). To help in following our necessarily abbreviated derivation of the equations, we advise the reader to consult § 2.3 of Paper I.

Figure 1, a slightly modified version of Figure 4 of Paper I, shows the representative patch in more detail. We let γ denote the surface tilt, i.e., the angle between the patch normal $\hat{\boldsymbol{n}}$ and the radial direction from the star $\hat{\boldsymbol{r}}$. The upper and lower faces, i.e., those depicted with the largest areas, coincide with the inner and outer shock fronts. The narrow faces to the left and right of the upper one trace loci of constant polar angle θ, while the remaining two have fixed ϕ. Note that the length Δs is a small increment of the global coordinate s measuring distance along the shell from the pole to the equatorial plane. Inspection of Figure 1 shows that $\Delta s = R \sec\gamma \Delta\theta$ and that the patch width is $\Delta w = R \sin\theta \Delta\phi$. The surface area of either the upper or lower face is $\Delta s \Delta w = \mathscr{A} \Delta\theta \Delta\phi$, and the total patch volume is $\Delta s \Delta w \Delta n = \mathscr{A} \Delta\theta \Delta\phi \Delta n$. Here Δn (called Δh in Paper I) is the patch thickness. The factor $\mathscr{A}$ is given by

$$\mathscr{A} = R^2 \sin\theta \sec\gamma \ . \tag{10}$$

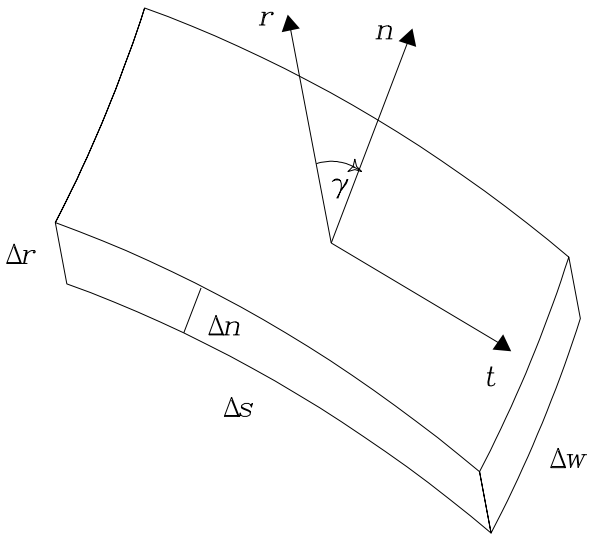

FIG. 1.—Element of the shell, with normal and tangential directions shown. The angle γ is measured clockwise from the radial to the normal direction. The shell thickness is Δn, while the arc length at constant azimuthal angle is Δs. The azimuthal width of the patch is $\Delta w = R \sin\theta \Delta\phi$. The length of the chord slicing the shell at constant (θ, ϕ) is $\Delta r = \Delta n \sec\gamma$.

For a mathematical description of the shell evolution, we let $R = R(\theta, \phi, t)$ be a dependent variable. Then the tilt angle γ is given by $\tan\gamma = -R'/R$, where $R' \equiv \partial R/\partial\theta$. During the evolution, we want the sides of our patch to retain fixed angular positions in θ and ϕ. On the other hand, we allow the upper and lower surfaces to move in and out radially, in order to follow expansion or contraction of the shell. Let us denote by (u_r, u_θ, u_ϕ) the velocity of matter within the shell. (Note the lack of additional subscripts, which we use to denote wind or infall.) The velocity component of this fluid pointing along the patch normal is

$$u_n = u_r \cos\gamma + u_\theta \sin\gamma \ . \tag{11}$$

Now shell expansion gives the patch itself a normal velocity

$$v_n = \frac{\partial R}{\partial t} \cos\gamma \ . \tag{12}$$

Our kinematical constraint on the patch motion is simply $u_n = v_n$. Combining equations (11) and (12), we find

$$\frac{\partial R}{\partial t} = u_r + u_\theta \tan\gamma \ . \tag{13}$$

Proceeding to the dynamical equations, we first derive an expression for $\Delta\dot{Q}$, the rate of change of any physical quantity within the patch. Let q denote the volume density of this quantity. This density may change with time, as may the patch volume. We thus have

$$\Delta\dot{Q} = \frac{\partial}{\partial t}(q \Delta n \Delta s \Delta w) = \frac{\partial}{\partial t}(\mathscr{A} q \Delta n) \Delta\theta \Delta\phi \ , \tag{14}$$

where the partial derivative is at fixed θ and ϕ.

The change in our quantity comes in part from advection into and out of the patch. The rate here depends on both the wind and infall velocities, as well as those within the patch itself. Note that the relevant wind and infall velocities are the normal components *relative to the patch*, since the latter has the normal velocity u_n. Let q_w and q_i be the density of the quantity in the wind and infall, respectively. Then these flows make an *external* contribution to $\Delta\dot{Q}$:

$$\begin{aligned} \Delta\dot{Q}_{\rm ext} &= \left[(u_{w,n} - u_n) q_w - (u_{i,n} - u_n) q_i\right] \Delta s \Delta w \\ &= \mathscr{A}\left(u'_{w,n} q_w - u'_{i,n} q_i\right) \Delta\theta \Delta\phi \ , \end{aligned} \tag{15}$$

where we have used primes for the relative normal velocities.

We must also account for the *internal* contribution to advection, i.e., the effect of flow within the shell. Part of this flow is due to motion in the θ-direction. Noting that the radial thickness of the shell is $\Delta r = (\Delta n) \sec\gamma$, Figure 1 shows that

$$\begin{aligned} \Delta\dot{Q}_{{\rm int},\theta} &= (u_\theta q \Delta r \Delta w)_{\theta - \Delta\theta/2} - (u_\theta q \Delta r \Delta w)_{\theta + \Delta\theta/2} \\ &= -\frac{\partial}{\partial\theta}\left(\mathscr{A} \frac{u_\theta q \Delta n}{R}\right) \Delta\theta \Delta\phi \ . \end{aligned} \tag{16}$$

The final contribution to advection stems from the

ϕ-velocity. Here we find

$$\Delta\dot{Q}_{\mathrm{int},\phi} = \left(u_\phi q \Delta s \Delta n\right)_{\phi-\Delta\phi/2} - \left(u_\phi q \Delta s \Delta n\right)_{\phi+\Delta\phi/2} = -u_\phi R \sec\gamma \frac{\partial q}{\partial \phi} \Delta n \Delta\theta \Delta\phi \ . \quad (17)$$

Apart from notation, this equation is identical to equation (18) of Paper I.

We now sum all the advective terms to form $\Delta\dot{Q}_{\mathrm{adv}}$. Combining equations (15)–(17), we have

$$\Delta\dot{Q}_{\mathrm{adv}} = \left\{ -\frac{\partial}{\partial\theta}\left(\mathscr{A}\frac{u_\theta}{R} q \Delta n\right) + \mathscr{A}\left[u'_{w,n} q_w - u'_{i,n} q_i - \frac{u_\phi}{\varpi}\frac{\partial}{\partial\phi}(q\Delta n)\right]\right\} \Delta\theta\Delta\phi \ , \quad (18)$$

where $\varpi \equiv R\sin\theta$ is the cylindrical radius.

In order to express mass conservation, we let q be the mass density ρ. Note that this quantity, like the others we shall be considering, is formally infinite in the limit $\Delta n \to 0$, whereas $\rho\Delta n$ is the finite surface density σ. Since there are no sources or sinks of mass, we demand that $\Delta\dot{Q} = \Delta\dot{Q}_{\mathrm{adv}}$. We find

$$\frac{\partial}{\partial t}(\mathscr{A}\sigma) + \frac{\partial}{\partial\theta}\left(\mathscr{A}\frac{\sigma u_\theta}{R}\right) = \mathscr{A}\left(\rho_w u'_{w,n} - \rho_i u'_{i,n}\right) . \quad (19)$$

Turning to momentum, we first note that the magnitude of the gravitational force on the patch is $\Delta F_g = GM_*\sigma\mathscr{A}\Delta\theta\Delta\phi/R^2$. This force would increase the momentum within the patch even if there were no advection. Suppose we choose our patch to be located at $\phi = 0$ in the global, spherical coordinate system. Then the Cartesian components of the gravitational force become $\Delta F_{g,x} = -\Delta F_g \sin\theta$, $\Delta F_{g,y} = 0$, and $\Delta F_{g,z} = -\Delta F_g \cos\theta$. The physical conservation law is most directly expressed in terms of Cartesian coordinates. In the x-momentum equation, we let $q = \rho u_x$ in equations (14) and (18) and demand that $\Delta\dot{Q} = \Delta\dot{Q}_{\mathrm{adv}} + \Delta F_{g,x}$. For the patch centered on $\phi = 0$, $u_x \approx u_\varpi$ and $\partial u_x/\partial\phi \approx -u_\phi$. Here u_ϖ is the cylindrical radial component of velocity. We obtain

$$\frac{\partial}{\partial t}(\mathscr{A}\sigma u_\varpi) + \frac{\partial}{\partial\theta}\left(\mathscr{A}\frac{\sigma u_\theta u_\varpi}{R}\right) = \mathscr{A}\left(\rho_w u'_{w,n} u_{w,\varpi} - \rho_i u'_{i,n} u_{i,\varpi} + \frac{\sigma u_\phi^2}{\varpi} - \frac{GM_*\sigma}{R^2}\sin\theta\right) . \quad (20)$$

The y-component of momentum conservation is simpler since $\Delta F_{g,y} = 0$. We now let $q = \rho u_y$ and use $u_y \approx u_\phi$ and $\partial u_y/\partial\phi \approx u_\varpi$ to find

$$\frac{\partial}{\partial t}\left(\mathscr{A}\sigma u_\phi\right) + \frac{\partial}{\partial\theta}\left(\mathscr{A}\frac{\sigma u_\theta u_\phi}{R}\right) = \mathscr{A}\left(\rho_w u'_{w,n} u_{w,\phi} - \rho_i u'_{i,n} u_{i,\phi} - \frac{\sigma u_\phi u_\varpi}{\varpi}\right) . \quad (21)$$

We may obtain a simpler form of this ϕ-force equation by instead writing it in terms of the z-component of angular momentum. First note that using equation (13), we have the relation $\partial\varpi/\partial t + (u_\theta/R)\partial\varpi/\partial\theta = u_\varpi$. Multiplying this equation by $\mathscr{A}\sigma u_\phi$ and adding it to ϖ times equation (21), we obtain

$$\frac{\partial}{\partial t}\left(\mathscr{A}\varpi\sigma u_\phi\right) + \frac{\partial}{\partial\theta}\left(\varpi\mathscr{A}\frac{\sigma u_\theta u_\phi}{R}\right) = \mathscr{A}\varpi\left(\rho_w u'_{w,n} u_{w,\phi} - \rho_i u'_{i,n} u_{i,\phi}\right) . \quad (22)$$

Similarly, the z-force equation is obtained using $q = u_z$:

$$\frac{\partial}{\partial t}(\mathscr{A}\sigma u_z) + \frac{\partial}{\partial\theta}\left(\mathscr{A}\frac{\sigma u_\theta u_z}{R}\right) = \mathscr{A}\left(\rho_w u'_{w,n} u_{w,z} - \rho_i u'_{i,n} u_{i,z} - \frac{GM_*\sigma}{R^2}\cos\theta\right) . \quad (23)$$

We have seen that beginning with Cartesian components of velocity, the azimuthal symmetry of the problem leads naturally to equations in terms of the cylindrical components of velocity. However, for a radial driving wind, it will be most useful to use spherical components. By taking linear combinations of equations (20) and (23) and substituting $u_\varpi = u_r\sin\theta + u_\theta\cos\theta$ and $u_z = u_r\cos\theta - u_\theta\sin\theta$, we may recast them in terms of the velocities u_r and u_θ:

$$\frac{\partial}{\partial t}(\mathscr{A}\sigma u_r) + \frac{\partial}{\partial\theta}\left(\mathscr{A}\frac{\sigma u_\theta u_r}{R}\right) = \mathscr{A}\left(\rho_w u'_{w,n} u_{w,r} - \rho_i u'_{i,n} u_{i,r} + \frac{\sigma u_\phi^2}{R} - \frac{GM_*\sigma}{R^2}\right) , \quad (24)$$

$$\frac{\partial}{\partial t}(\mathscr{A}\sigma u_\theta) + \frac{\partial}{\partial\theta}\left(\mathscr{A}\frac{\sigma u_\theta u_\theta}{R}\right) = \mathscr{A}\left(\rho_w u'_{w,n} u_{w,\theta} - \rho_i u'_{i,n} u_{i,\theta} + \frac{\sigma u_\phi^2\cot\theta}{R}\right) . \quad (25)$$

Previously, Giuliani (1982) derived an equivalent set of equations, including magnetic fields, but without accounting for gravity or rotation.

2.4. *Time-dependent Equations: Lagrangian Form*

In practice, it is simplest to solve the evolutionary equations by recasting them in Lagrangian form. Consider first the comoving derivative of any quantity Q within the shell. In the Eulerian description we have used until now, Q is a function of t, θ, and ϕ. It also depends implicitly on radius, since, at fixed θ and ϕ, the radius R varies with time. The comoving derivative is therefore

$$\frac{DQ}{Dt} = \frac{\partial Q}{\partial t} + \frac{u_\theta}{R}\frac{\partial Q}{\partial\theta} + \frac{u_\phi}{R\sin\theta}\frac{\partial Q}{\partial\phi} \ . \quad (26)$$

We now let Q be, in turn, the radial and angular positions of a moving fluid element that constitutes part of the shell. This element is no longer constrained in θ and ϕ, as was our patch. Retaining the old notation for these coordinates, now serving as dependent variables, we substitute into equation (26) to find

$$\frac{DR}{Dt} = u_r \ , \quad (27)$$

$$\frac{D\theta}{Dt} = \frac{u_\theta}{R} \ , \quad (28)$$

$$\frac{D\phi}{Dt} = \frac{u_\phi}{R\sin\theta} \ . \quad (29)$$

In deriving equation (27), we have used both equation (13) and the definition of γ in terms of R'. Equations (27)–(29)

describe both the expansion of the shell and tangential motion along its surface. We next substitute for Q in equation (26) the quantity $\mathscr{A}\sigma$. After utilizing equation (19), we arrive at the Lagrangian expression for mass conservation, which we may write as

$$\frac{D[\ln(\mathscr{A}\sigma)]}{Dt} = \frac{\rho_w u'_{w,n} - \rho_i u'_{i,n}}{\sigma} - \frac{\partial}{\partial\theta}\left(\frac{u_\theta}{R}\right) . \quad (30)$$

To obtain the r- and θ-components of the force equation, as well as the expression for angular momentum conservation, we substitute for Q the quantities u_r, u_θ, and ϖu_ϕ, respectively. We then use our Eulerian conservation laws and equation (30) in each case to find

$$\frac{Du_r}{Dt} = \frac{\rho_w u'_{w,n} u'_{w,r} - \rho_i u'_{i,n} u'_{i,r}}{\sigma} + \frac{u_\theta^2}{R} + \frac{l^2 \sin\theta}{\varpi^3} - \frac{GM_*}{R^2} , \quad (31)$$

$$\frac{Du_\theta}{Dt} = \frac{\rho_w u'_{w,n} u'_{w,\theta} - \rho_i u'_{i,n} u'_{i,\theta}}{\sigma} - \frac{u_r u_\theta}{R} + \frac{l^2 \cos\theta}{\varpi^3} , \quad (32)$$

$$\frac{Dl}{Dt} = \frac{\rho_w u'_{w,n} l'_w - \rho_i u'_{i,n} l'_i}{\sigma} . \quad (33)$$

Here we have let $l \equiv \varpi u_\phi$ be the z-component of specific angular momentum and have further defined

$$l'_w \equiv \varpi\left(u_{w,\phi} - u_\phi\right) , \quad (34)$$

$$l'_i \equiv \varpi\left(u_{i,\phi} - u_\phi\right) . \quad (35)$$

Equations (27)–(29) and (31)–(33) may be summarized in vector form as

$$\frac{D\boldsymbol{R}}{Dt} = \boldsymbol{u} , \quad (36)$$

$$\frac{D\boldsymbol{u}}{Dt} = \frac{\rho_w u'_{w,n} \boldsymbol{u}'_w - \rho_i u'_{i,n} \boldsymbol{u}'_i}{\sigma} - \frac{GM_*}{R^2}\hat{\boldsymbol{r}} . \quad (37)$$

As expected, the acceleration of the fluid element depends on both the radial force of gravity and the input of momentum from wind and infall. Note finally that the mass conservation equation (30) contains an Eulerian derivative on the right-hand side, so that our equations are not in purely Lagrangian form. Indeed, the normal components of wind and infall speed that enter equations (30)–(33) also require, through the angle γ, the Eulerian derivative $\partial R/\partial\theta$. In practice, this mixed character of the equations and the fact that θ acts as both a dependent and independent variable present no special difficulty for integration.

3. METHOD OF SOLUTION

Equations (27)–(33) fully describe the motion of a fluid element within the shell. Because the latter is axisymmetric, there is no need to track the ϕ-coordinate, and we may ignore equation (29). We treat the others effectively as ordinary differential equations in time and use them to follow a collection of 50 discrete points that represents our shell. We evaluate the cross derivatives $\partial R/\partial\theta$ and $\partial(u_\theta/R)/\partial\theta$, by numerically differencing R and u_θ/R. This method has been employed previously for the similar problem of steady state, nonaxisymmetric bow shocks and expanding supershells (Mac Low & McCray 1988; Bandiera 1993) and works well provided that the spacing between adjacent trajectories is fine enough to determine numerical derivatives.

For each of the 50 points, we integrated the equations in time using a fifth-order Runge-Kutta scheme. Cross derivatives were obtained at each point by using the two nearest neighbors and were thus second-order accurate. Since the points move in a manner dictated by the local fluid velocity, they are unevenly spaced in angle. In practice, we approximated the shell segment by fitting a circular arc through each triad of points. The cross derivatives at the middle point were then obtained analytically from this curve.

As the shell evolved in time, some of its representative points inevitably drifted toward the equatorial plane. In addition, points could move so close together that there was little variation in the intervening space. In either circumstance, we removed a point from the original set. We immediately replaced it with another, which we introduced at the part of the shell that was most sparsely covered. We always retained one point on the symmetry axis, where the boundary conditions $R' = u_\theta = u_\phi = 0$ were applied. Here the mass equation was written in modified form to account for the vanishing of the $\sin\theta$ factor within $\mathscr{A}$.

We tested our code on three problems with known, analytic solutions. They include (1) an expanding, spherical shell driven by an isotropic wind, (2) a shell driven by an angle-dependent wind within an r^{-2} density distribution (Shu et al. 1991), and (3) the bow shock created by the wind from a star that is moving into a uniform medium. The first two tests confirmed the code to better than 1% accuracy in a nonsteady situation. For the last problem, Wilkin (1996) found analytic solutions for the steady state shell configuration, including the surface density and flow velocity along the shell. Figure 2 shows the expansion of our time-dependent bow shock as it approaches the steady state endpoint. We have checked

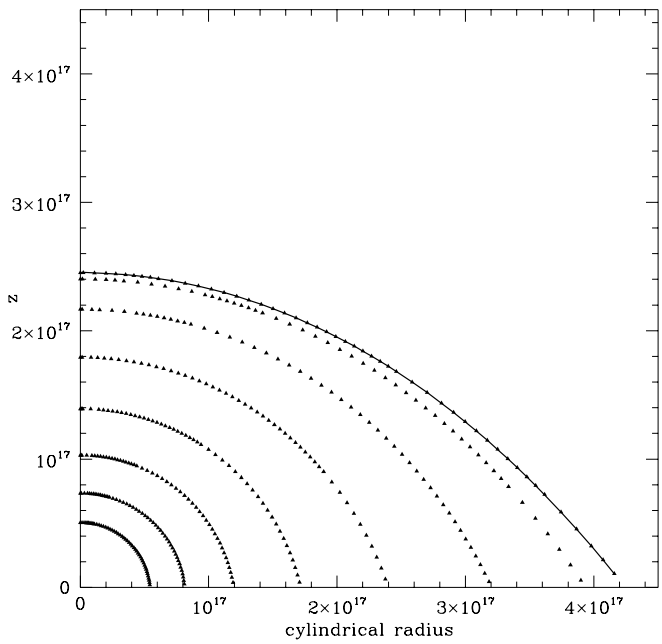

FIG. 2.—Approach of the shell to the steady state bow shock solution. In the frame of the star, located at the origin, the ambient medium moves with velocity $-V_*\hat{\boldsymbol{z}}$. The initially spherical shell began at $3R_{\rm sun}$, much smaller than the standoff radius $R_0 = 2.45 \times 10^{17}$ cm. Solutions are shown for elapsed time increasing by a factor of 2 from 1/32 to 4 times the crossing time R_0/V_*. Triangles denote grid points, while the analytic, steady state solution is given by the solid curve.

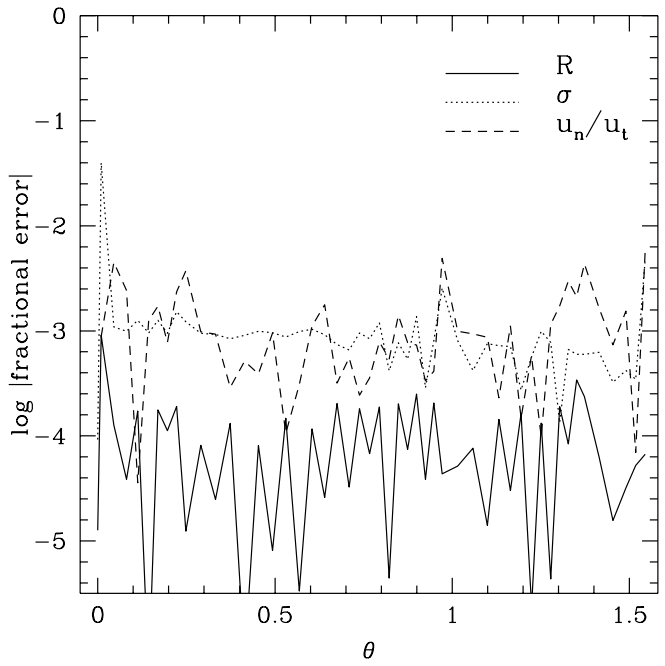

FIG. 3.—Fractional errors for the bow shock test case after reaching near-equilibrium. Because the normal velocity vanishes in steady state, the quantity u_n/u_t refers to the normal velocity of the grid points divided by the analytic solution for the tangential velocity.

that the approach to equilibrium agrees with the calculations of Giuliani (1982).

Figure 3 compares a number of quantities in the analytic solution with our numerical results, at a time when equilibrium has been reached. The fractional errors are between 10^{-2} and 10^{-4}, except close to the pole. Judging from the three tests, we believe that our code is capable of tracking all variables in the time-dependent shell to within an accuracy of 1%–2%.

4. INSTABILITY OF THE QUASI-STEADY SOLUTION

Before displaying our fully time-dependent results, we first discuss the quasi-steady solutions obtained in Paper I.[1] These shells are in dynamical equilibrium, with gravity and the infall ram pressure opposing the outward ram pressure from the wind. Because gravity plays a dominant role, we suspected that the shells might be dynamically unstable (see § 4 of Paper I). We now demonstrate this fact both analytically and numerically.

4.1. *Analytical Argument*

We first examine the stability in the region of the polar axis. This approach extracts the basic physics while bypassing a full modal analysis, such as that done for wind bow shocks by Dgani, Van Buren, & Noriega-Crespo (1996). The total radial force per unit area acting on the shell near the axis is

$$F_r = \rho_w V_w^2 - \rho_i u_{i,r}^2 - \frac{GM_*\sigma}{R^2} \ . \tag{38}$$

Note that we have omitted centrifugal terms, which are vanishingly small near the pole.

The condition of normal force balance is that $F_r(R_0) = 0$, where R_0 is the shell's equilibrium polar radius. We now imagine perturbing the shell and examine the resulting change in F_r. For this purpose, we consider the lowest order oscillation mode of the shell, i.e., its breathing mode. We find the altered wind density ρ_w from equation (8) and the infall density ρ_i and velocity $u_{i,r}$ from equations (6) and (3), respectively. For the latter two quantities, we specialize to the pole by setting $\theta_0 = \theta = 0$. To obtain the perturbed value of the mass density σ, we ignore any additional mass swept up by the shell during its oscillation. Thus, to conserve mass, we write $\sigma = \sigma_0 R_0^2/R^2$, where σ_0 is the equilibrium value. Equation (38) then becomes

$$F_r = \frac{\dot{M}_w V_w}{4\pi R^2} - \frac{\dot{M}_i}{4\pi R^2}\left(\frac{2GM_*}{R}\right)^{1/2}\frac{1}{1+2\zeta} - \frac{GM_*\sigma_0 R_0^2}{R^4} \ , \tag{39}$$

where $\zeta \equiv R_{\rm cen}/R$. Note that we have also neglected alterations to the surface density due to the *perturbation* in the tangential motion. We showed in Paper I that such motion is generally small compared to the wind and infall speeds.

We next nondimensionalize equation (39) by dividing through by $\dot{M}_w V_w/4\pi R_0^2$. Again employing subscripts for equilibrium values, we have

$$\mathscr{F}_r = \left(\frac{R}{R_0}\right)^{-2} - f_i\left(\frac{R}{R_0}\right)^{-5/2}\frac{1+2\zeta_0}{1+2\zeta} - f_g\left(\frac{R}{R_0}\right)^{-4} \ . \tag{40}$$

The constants f_i and f_g are the nondimensional (fractional) contributions of the infall and gravitational forces, respectively, at the equilibrium position. These are given by

$$f_i = \frac{\dot{M}_i}{\dot{M}_w}\left(\frac{2GM_*}{V_w^2 R_0}\right)^{1/2}\frac{1}{1+2\zeta_0} \ , \tag{41}$$

$$f_g = \frac{4\pi GM_*\sigma_0}{\dot{M}_w V_w} \ . \tag{42}$$

The requirement that R_0 be an equilibrium radius means that $f_g = 1 - f_i$. Thus, we may eliminate f_g from equation (40). Writing $R/R_0 = 1 + \delta$ and recalling that $\zeta \propto 1/R$, we linearize in δ to find the small radial force due to the oscillation:

$$\mathscr{F}_r \approx \left[2 - f_i\frac{3+10\zeta_0}{2(1+2\zeta_0)}\right]\delta \ . \tag{43}$$

We see that there is a critical value for f_i:

$$f_{i,\rm crit} = \frac{4(1+2\zeta_0)}{3+10\zeta_0} \ . \tag{44}$$

If the actual f_i in the equilibrium solution exceeds $f_{i,\rm crit}$, then the radial force is directed opposite to the displacement; i.e., the shell is stable (or overstable). Conversely, $f_i < f_{i,\rm crit}$ implies dynamic instability. The *minimum* value of $f_{i,\rm crit}$, that for infinite ζ_0, is 0.8; that is, at least 80% of the confining

[1] We draw the reader's attention to two typographical errors in Paper I. Equation (70) should have an overall minus sign on the right-hand side, and equation (72) should read $\epsilon \equiv \alpha \sin\theta - \tau\Phi_m^2/R\Phi_t \cos\gamma$.

force must come from the infall ram pressure, rather than gravity, to ensure stability.

We now return to the exact results of Paper I. There we found f_i to be

$$f_i = \left\{ 1 + \frac{3}{4} \frac{(1+2\zeta_0)[1+\alpha(1+2\zeta_0)]^2}{\zeta_0 + \sqrt{\zeta_0^2 + 3\zeta_0/8}} \right\}^{-1} , \quad (45)$$

where $\alpha \equiv \dot{M}_w/\dot{M}_i$ is the ratio of wind to infall mass transfer rates. This result is taken from equation (60) of Paper I, where the three terms of that equation correspond, from left to right, to the normal force due to wind, infall, and gravity, respectively. For a fixed value of ζ_0, decreasing α increases f_i. Thus, we consider the limit $\alpha \to 0$, to obtain the largest possible value of f_i. If we set $\alpha = 0$ in equation (45), then f_i monotonically increases with ζ_0. The maximum of f_i occurs in the limit $\zeta_0 \to \infty$, $\alpha \to 0$, in which case $f_i = \frac{4}{7}$. Since this is substantially less than the minimum value of f_i necessary for stability, we conclude that there are no combinations of α and ζ_0 such that the shell is stable. While this analysis is based on conditions near the symmetry axis, the small contribution of centrifugal effects at larger angles (§ 3.3 of Paper I) suggests that the same result should hold throughout the shell. One might argue that the steady state solution might nevertheless be achieved in some average sense. While this has been found to be true for isothermal bow shocks (Blondin & Koerwer 1998; Raga et al. 1997), the calculations we next describe indicate that this is not the case in our problem.

4.2. *Numerical Demonstration*

We next use our time-dependent code to evolve shells starting near the steady state conditions derived in Paper I. The latter calculation gives us the run of R, σ, u_t, u_ϕ for a grid of θ-values. We first verified the validity of the steady state solutions, checking that the net normal force on a fluid element is equal to the normal component of the centrifugal force it experiences. Despite this balance, the shells do not stay in their initial configuration but evolve quickly. Shells begun at a size slightly larger than equilibrium expand, while those of slightly smaller size collapse, as expected by the analytical argument. A representative example is shown in Figure 4. The innermost two curves are polar radii for shells distorted slightly inward from equilibrium, while the outermost two curves represent shells begun slightly beyond the equilibrium radius. All other quantities in the shell, such as the run of surface density with polar angle, were initially the same as for steady state. The equilibrium solution shown is that of the critical (innermost) model for $\alpha = 0.1$ shown in Figure 9 of Paper I. The slightly shrunken, collapsing shell quickly accelerates to free-fall speed, while the expanding structure eventually decelerates at large radius as a momentum-conserving snowplow. The analytic argument of the preceding section, together with these and similar numerical experiments, shows convincingly that the quasi-steady shells are dynamically unstable. This basic result motivates our current study, where we consider the shell evolution as an explicitly time-dependent, initial value problem.

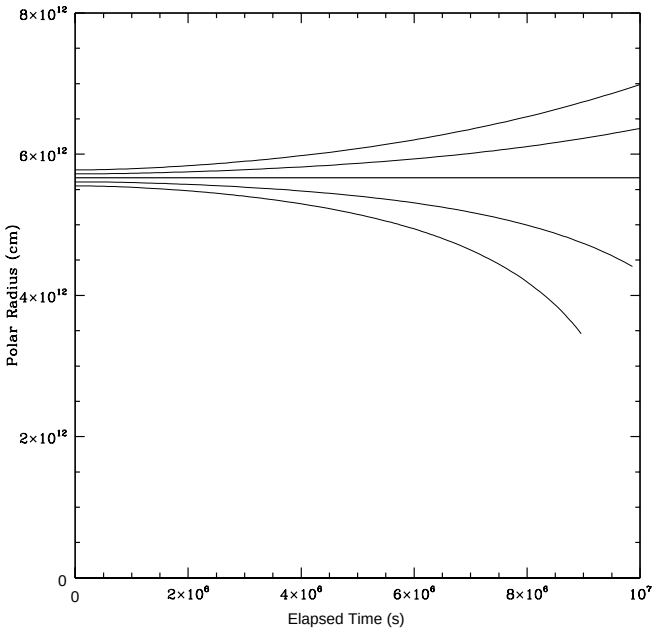

FIG. 4.—Instability of an initial steady state solution: polar radius vs. time for shells starting close to the steady state solution of Paper I. Shells begun at slightly smaller radius collapse, while shells begun at slightly larger radius expand indefinitely. The equilibrium radius is shown (*boldface*) for the solution corresponding to $\alpha = 0.1$, $\zeta_0 = 2.45$.

5. TIME-DEPENDENT EVOLUTION: BASIC CONSIDERATIONS

5.1. *Initial Conditions*

We now wish to follow the motion of the shell from its launch near the protostellar surface. Our shell is initially spherical and massless, with radius equal to that of the protostar, R_*. As the structure evolves, it receives mass from both the wind and infall. Thus, even at launch, there are well-defined values for all the physical quantities of interest. Note, however, that the momentum equation (37) is singular if σ vanishes. The initial velocity is found by setting the corresponding numerator to zero:

$$\rho_w u'_{w,n}(\boldsymbol{u}_w - \boldsymbol{u}_0) - \rho_i u'_{i,n}(\boldsymbol{u}_i - \boldsymbol{u}_0) = 0 . \quad (46)$$

Here we have explicitly written the vector velocity differences. We define $\lambda \equiv -\rho_i u'_{i,n}/\rho_w u'_{w,n}$, which is the ratio of mass fluxes from the wind and infall onto the shell. Then equation (46) becomes

$$\boldsymbol{u}_0 = \frac{\boldsymbol{u}_w + \lambda \boldsymbol{u}_i}{1+\lambda} . \quad (47)$$

To find λ explicitly, we take the normal component of equation (46), obtaining $\rho_w u'^2_{w,n} = \rho_i u'^2_{i,n}$. Defining $\eta \equiv \rho_i/\rho_w$ and taking the square root of both sides, we have

$$(u_{w,n} - u_{0,n}) = \eta^{1/2}(u_{0,n} - u_{i,n}) . \quad (48)$$

In obtaining equation (48), we have accounted for the fact that $u_{i,n} < u_{0,n} < u_{w,n}$. Equation (48) implies

$$\lambda = \eta^{1/2} , \quad (49)$$

which yields the final result

$$\boldsymbol{u}_0 = \frac{\boldsymbol{u}_w + \eta^{1/2}\boldsymbol{u}_i}{1+\eta^{1/2}} \ . \tag{50}$$

In equation (50), both $\boldsymbol{u}_i$ and η depend on θ. The normal component of this equation represents the balance of wind and infall ram pressures in the frame of the shell. This result is a generalization of the well-known formula for the speed of the planar bow shock driven by a steady jet (e.g., Blandford, Begelman, & Rees 1984). In our case, however, the "ambient" matter is in nonuniform motion with velocity $\boldsymbol{u}_i$. For a dense wind $\eta \ll 1$, the shell tends to the wind speed, while for a rarefied wind with $\eta \gg 1$, the shell collapses at the infall speed.

To derive the initial rate at which mass is being swept up, we use equation (30):

$$\begin{aligned} \frac{D\sigma}{Dt} \approx \frac{\partial \sigma}{\partial t} &\equiv \dot{\sigma}_0 \\ &= \rho_w u'_{w,n} - \rho_i u'_{i,n} \ , \end{aligned} \tag{51}$$

where we have dropped terms from equation (30) that vanish with σ. The right-hand side of equation (51) is to be evaluated using equation (50) for the shell's initial velocity.

Our calculation requires values for the stellar radius R_*, wind speed $V_w \equiv |\boldsymbol{u}_w|$, and mass-loss rate $\dot{\boldsymbol{M}}_w$. The distribution of infalling matter is specified by t, the time since the start of collapse, together with the sound speed a_0 and rotation rate Ω_0 of the parent dense core. Thus, there are six dimensional parameters. In principle, the protostellar radius is not independent of the others but should be obtained from stellar evolution theory (e.g., Stahler 1988). However, we will simply adopt a characteristic protostellar radius and show how the results scale with this and other choices of the dimensional parameters.

5.2. *Nondimensional Parameters and Equations*

To reduce the number of runs needed to explore parameter space, we cast the equations in nondimensional form. There are two timescales of interest: an *evolutionary* and a *dynamical* one. The first is the time over which the infall itself changes appreciably. In terms of the dimensional parameters listed previously, we define

$$t_{\rm ev} \equiv \left(\frac{R_*}{a_0 \Omega_0^2} \right)^{1/3} \ . \tag{52}$$

According to equation (10) of Stahler et al. (1994), $t_{\rm ev}$ is, to within a factor of order unity, the time after start of collapse when the centrifugal radius associated with infall attains the value R_*.

We find the dynamical time by first assigning units of length and velocity. The first is R_*, and the second is the Keplerian speed at the stellar surface. Since the characteristic stellar mass is $\dot{\boldsymbol{M}}_i t_{\rm ev}$, we have

$$V_* \equiv \frac{a_0^{4/3}}{R_*^{1/3}\Omega_0^{1/3}} \ , \tag{53}$$

where we have left out the factor of m_0 entering equation (1) for $\dot{\boldsymbol{M}}_i$. The dynamical time is now defined as R_*/V_*, or

$$t_{\rm dyn} \equiv \frac{R_*^{4/3}\Omega_0^{1/3}}{a_0^{4/3}} \ . \tag{54}$$

Note finally that the mass of the shell, after a dynamical time, is of magnitude $\dot{\boldsymbol{M}}_i t_{\rm dyn}$. We formally define our mass unit as

$$M_{\rm dyn} \equiv \frac{a_0^3}{4\pi G \Omega_0} \left(\frac{R_* \Omega_0}{a_0} \right)^{4/3} \ . \tag{55}$$

Here again we have left out the factor of m_0 and have introduced a factor of 4π for later convenience.

All physical variables can be written as dimensionless factors times appropriate combinations of R_*, $t_{\rm dyn}$, and $M_{\rm dyn}$. Additionally, certain nondimensional ratios enter the final equations. One involves the mass transport rates in the wind and infall:

$$\alpha \equiv \frac{\dot{\boldsymbol{M}}_w}{\dot{\boldsymbol{M}}_i} \ . \tag{56}$$

In this study, we only consider values of α less than unity. A second ratio is the wind speed divided by our dynamical unit of velocity:

$$\nu \equiv \frac{V_w}{V_*} \ . \tag{57}$$

Assigning canonical values of the dimensional parameters $a_0 = 0.2\ {\rm km\ s^{-1}}$, $\Omega_0 = 2 \times 10^{-14}\ {\rm s^{-1}}$, and $R_* = 3\ R_\odot$, as well as a reference wind speed of 200 km s^{-1}, the reader may verify that ν is of order unity. The third key nondimensional ratio is the initial launch time of the shell in terms of $t_{\rm ev}$:

$$\tau_0 \equiv \frac{t_{\rm init}}{t_{\rm ev}} \ . \tag{58}$$

For $\tau_0 \ll 1$, the centrifugal radius has not yet reached the protostellar radius, and the infall conditions are those of nearly spherically symmetric free fall. For $\tau_0 \gg 1$, the initial launch is within the inner, anisotropic region of the infall. In order to compute the evolution of the shocked shell in dimensionless units, only the three nondimensional ratios α, ν, and τ_0 need to be specified.

Another obvious ratio is that of the dynamical and evolutionary timescales:

$$\begin{aligned} \epsilon &\equiv \frac{t_{\rm dyn}}{t_{\rm ev}} \\ &= \frac{R_* \Omega_0}{a_0} \ . \end{aligned} \tag{59}$$

This quantity is of order 10^{-7}. Since our calculations span only dynamical times, ϵ does not appear explicitly in the final, nondimensional equations (see below). Note that our previous physical units can be written as

$$V_* = \epsilon^{-1/3} a_0 \ , \tag{60a}$$

$$t_{\rm dyn} = \epsilon^{4/3} \Omega_0^{-1} \ , \tag{60b}$$

$$M_{\rm dyn} = \epsilon^{4/3} \frac{a_0^3}{4\pi G \Omega_0} \ . \tag{60c}$$

The nondimensional equations include various quantities related to the infall. These, in turn, depend on the time t since the start of collapse. Since our basic temporal unit is $t_{\rm dyn}$, we may write

$$t = \epsilon^{-1}\tau t_{\rm dyn} \ . \tag{61}$$

Here τ is the nondimensional evolutionary time, written in terms of $t_{\rm ev}$. In practice, the difference between τ and τ_0 is exceedingly small. Even if we were to evolve the shell for 10^4 dynamical times, τ would only change fractionally by order 10^{-3}. Thus, in the dynamical equations we treat τ as a constant and drop the unnecessary subscript on τ_0.

To complete our description of the nondimensional problem, we give the dimensionless forms of the remaining infall and wind quantities. We write the infall vector velocity in terms of the Keplerian speed as $\boldsymbol{u}_i = u_{\rm K}\boldsymbol{f}$, where $u_{\rm K} \equiv \sqrt{GM_*/R}$, and the components of $\boldsymbol{f}$ may be deduced from equations (3)–(5). Letting tildes denote nondimensional quantities (e.g., $\tilde{R} \equiv R/R_*$) and using $GM_* = m_0 a_0^3 t$, we obtain

$$\tilde{u}_{\rm K} = m_0^{1/2}\left(\frac{\tau}{\tilde{R}}\right)^{1/2} \ . \tag{62}$$

Similarly, the quantity ζ is given by

$$\zeta = m_0^3\frac{\tau^3}{16\tilde{R}} \ . \tag{63}$$

When the centrifugal radius equals the stellar radius, $\zeta = 1$ at the surface of the star. From the above equation, the corresponding nondimensional time τ is 2.54. The infall and wind densities in nondimensional form are

$$\tilde{\rho}_i = \frac{\tilde{S}_i}{\tilde{R}^2\tilde{u}_{\rm K}} \ , \tag{64}$$

$$\tilde{\rho}_w = \frac{\alpha}{\tilde{R}^2\nu} \ , \tag{65}$$

where the infall density shape function is

$$\tilde{S}_i^{-1} \equiv -f_r[1 + 2\zeta P_2(\cos\theta_0)] \ . \tag{66}$$

Dropping the tilde notation, the dimensionless form of the dynamical equations is

$$\frac{D\boldsymbol{R}}{Dt} = \boldsymbol{u} \ , \tag{67}$$

$$\frac{D[\ln(\mathscr{A}\sigma)]}{Dt} = \frac{1}{R^2\sigma}\left[\alpha\left(\cos\gamma - \frac{u_n}{\nu}\right) - S_i\left(f_n - \frac{u_n}{u_{\rm K}}\right)\right] - \frac{\partial}{\partial\theta}\left(\frac{u_\theta}{R}\right) \ , \tag{68}$$

$$\frac{D\boldsymbol{u}}{Dt} = \frac{1}{R^2\sigma}\left[\alpha\left(\cos\gamma - \frac{u_n}{\nu}\right)\boldsymbol{u}_w' - S_i\left(f_n - \frac{u_n}{u_{\rm K}}\right)\boldsymbol{u}_i'\right] - m_0\frac{\tau\hat{\boldsymbol{r}}}{R^2} \ . \tag{69}$$

Note again that only three parameters, the dimensionless ratios α, τ, and ν, enter the final equations.

In order to launch a shell, the driving wind speed must be sufficient to yield a shell velocity $u_r > 0$, which in turn implies that the wind ram pressure exceed the infall ram pressure at the stellar surface. In terms of our chosen units, we require $\nu > \nu_{\rm ram}$, where

$$\nu_{\rm ram} = \frac{\nu_{\rm esc}}{\alpha(1 + m_0^3\tau^3/8)} \tag{70}$$

is the value of ν that balances ram pressures at the stellar pole, and $\nu_{\rm esc} = (2m_0\tau)^{1/2}$ (see eq. [62]) is the escape speed at the stellar surface.

6. NUMERICAL RESULTS

6.1. *Breakout versus Recollapse*

Before discussing the details of our numerical results, we note that the mass of the shell typically will be dominated by the swept-up infall. In the limit of a stationary, spherical shell, the ratio of wind to infall contributions is α (<1), but outward motion of the shell further increases the fractional contribution of infall to the shell mass. Although our calculations conserve the z angular momentum of the incident, infalling gas, the centrifugal support of the shell is modest. The primary effect of infall angular momentum is to establish an asymmetric flow, which is then swept up by the expanding shell.

A sample evolutionary sequence is shown in Figures 5–7 for a typical choice of nondimensional parameters ($\alpha = \frac{1}{3}$, $\tau = 4$, $\nu = 4.7$). Here the results are displayed both nondimensionally and in physical units. For the latter, we assumed standard values of the dimensional quantities: $R_* = 3\ R_\odot$, $\Omega_0 = 2 \times 10^{-14}$ s^{-1}, $a_0 = 0.2$ km s^{-1}. These choices imply an accretion rate of $1.85 \times 10^{-6}\ M_\odot$ yr^{-1}, a time since protostar formation of 38,000 yr, and a wind speed of 159 km s^{-1}. The shell first elongates as it expands

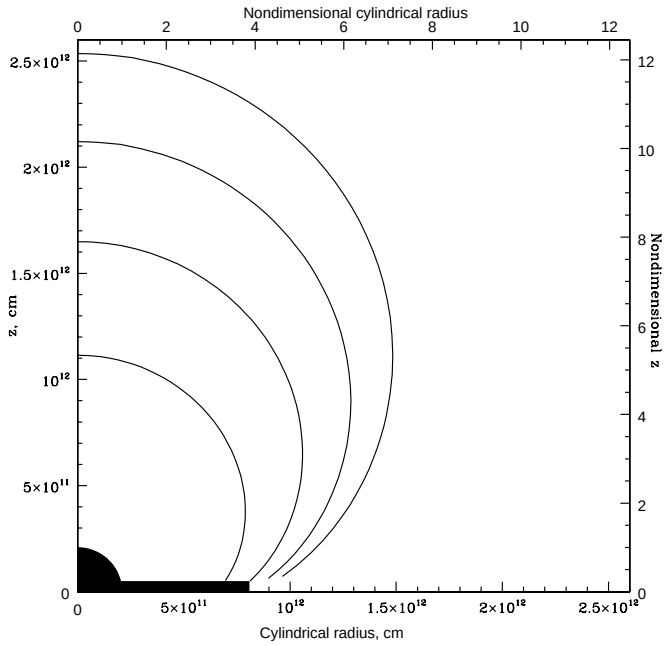

FIG. 5.—Time evolution of an escaping shell (early evolution), corresponding to $\alpha = \frac{1}{3}$, $\nu = 4.7$, and $\tau = 4.0$. The protostellar age since core formation is 3.8×10^4 yr. The shapes correspond to equal time intervals of 0.016 yr. The subsequent evolution of this shell is shown in the next two figures on a larger scale. The scale of the centrifugal radius is indicated by the disk. Lengths are in cm on the left and bottom axes, and in units of the stellar radius on the top and right axes.

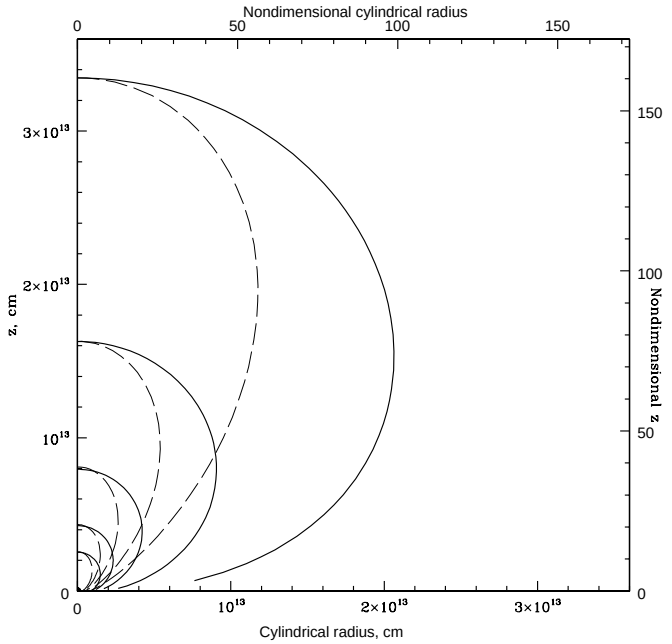

FIG. 6.—Time evolution of an escaping shell (further evolution), corresponding to the same parameters as Fig. 5, but for increasing times steps and on a larger scale. The innermost curve of this figure is the same as the outermost of that figure. However, the elapsed time increases by a factor of 2 with each curve: 4, 8, 16, 32, and 64 time units. The dashed curves represent an "equivalent" model driven by an asymmetric wind (see § 6.3).

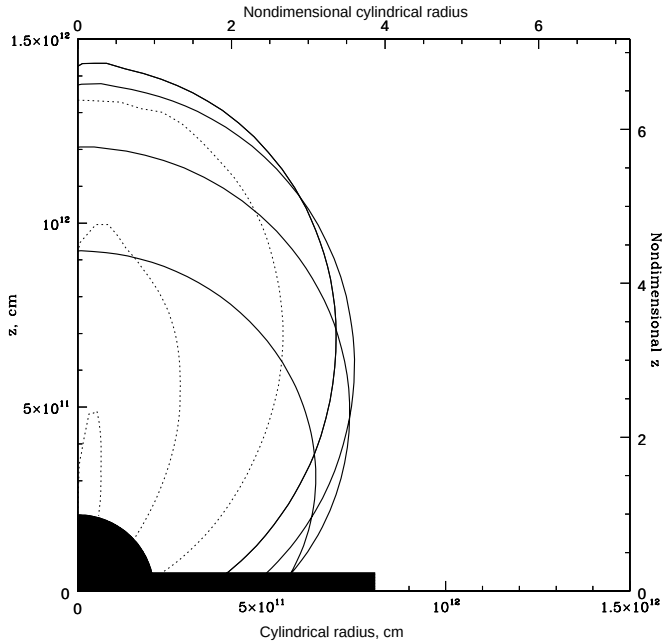

FIG. 8.—Time evolution of a recollapsing shell corresponding to $\alpha = \frac{1}{3}$, $\nu = 4.4$, and $\tau = 4.0$. The critical wind speed for these parameters is $\nu_{\rm crit} = 4.48$. Solid curves show the rising phase, while dotted curves display the subsequent recollapse. Shown for equal time intervals of $\frac{1}{4}$ is the time to reach the highest point along the z-axis, which is the same interval as the unit used in Fig. 5.

up to and beyond the disk radius, indicated in Figure 5. This outward motion never ceases, as the wind is able to drive back the infalling envelope in all directions. We refer to such an outcome as *breakout*. While at intermediate times (see Fig. 6) the shell is quite elongated and a bipolar geometry is obtained, at late times (Fig. 7) the shell takes on a more spherical appearance. In this spatial regime, well beyond the disk radius, the ambient density is also spherically symmetric.

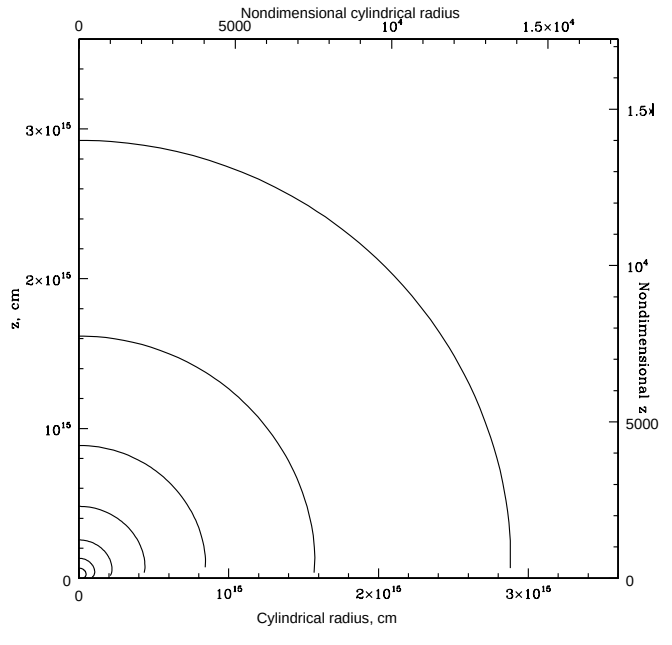

FIG. 7.—Time evolution of an escaping shell (late time), corresponding to the same parameters as Figs. 5 and 6. Here the shell has gone well beyond the centrifugal radius of the infall and is in the increasingly spherically symmetric infall region. Hence, the shell becomes more spherical as it sweeps up this material. The elapsed time doubles with each successive curve. The innermost here corresponds to 128 time units of Fig. 5, while the outermost is greater by a factor of 64 (8192 time units), which corresponds to 134 yr since launch.

Figure 8 shows that dramatically different results are obtained with very similar input parameters ($\alpha = \frac{1}{3}$, $\tau = 4$, $\nu = 4.4$). Dimensionally, the wind speed has now been lowered to 148 km s^{-1}. The shell initially rises as before, but it stalls and falls back to the star at nearly free-fall speed. As the shell plummets to the stellar surface, initial ripples are amplified; higher numerical resolution would be needed to follow this apparent instability. We will not be interested in such details, but only in whether or not the shell succeeds in driving back the infall. Shells that break out are typically quite smooth and regular. Even for those that recollapse, the structure is smooth up to the point of turnaround. Note that recollapse is caused primarily by gravity acting on the heavy shell, rather than infall ram pressure. Turning off gravity in the code, breakout is achieved for a wind speed less than half of that in Figure 8.

For those shells that do achieve breakout and have traveled far relative to the initial stellar radius, all quantities follow a power law determined by the slope in the infall density law. For $R_{\rm cen} \ll r \ll a_0 t$, $\rho_i \propto r^{-3/2}$, so the swept-up mass varies as $r^{3/2}$, while the shell's momentum grows linearly with time. The resulting momentum-driven snowplow has $R \propto t^{4/5}$ and $V_r \propto t^{-1/5}$.

6.2. *Critical Solutions*

We have mapped the parameter space of solutions as a function of α, τ, and ν. For a given value of α, the τ-ν plane is divided into three regions: one in which shells cannot even

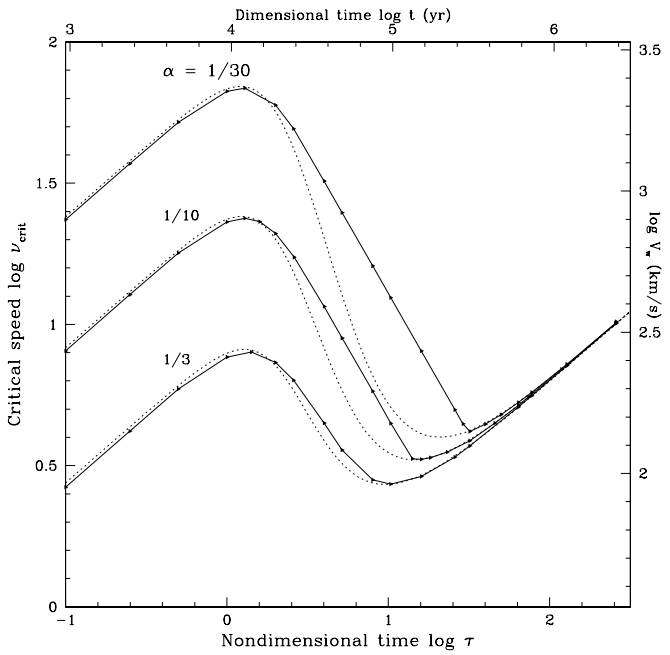

FIG. 9.—Minimum breakout wind speed vs. evolutionary time. The three loci (*solid curves*) correspond to three ratios, α, of the wind mass loss to infall accretion rate. For a given α, the region above the curve corresponds to breakout, while that below the curve corresponds to recollapse. An analytic fit to the numerical solutions is shown as dashed curves.

advance beyond the stellar surface, one in which the shell may initially rise but is pulled back, and one in which the shell breaks out. These solution regimes will be called the crushed wind, the trapped wind, and the escaping wind, respectively. In the τ-ν plane, the boundary between the crushed wind and the trapped wind is the locus $\nu_{\rm ram}(\alpha, \tau)$ given by equation (70), where infall and wind ram pressures balance at the stellar surface. We similarly denote by $\nu_{\rm crit}$ the minimum nondimensional wind speed necessary for breakout. Figure 9 plots this quantity as a function of time, for three representative values of α. Again, we display the results both nondimensionally and in physical units, employing our fiducial input parameters. Table 1 also lists values of $\nu_{\rm crit}$ at selected times. Returning to the figure, we see that, at very early times, $\nu_{\rm crit}$ increases as $\tau^{1/2}$ and is also *inversely* proportional to α. At intermediate times such that $R_{\rm cen} \sim R_*$, the centrifugal deflection of infalling gas lowers the infall density, and $\nu_{\rm crit}$ consequently falls. Once again, $\nu_{\rm crit}$ at any time during this epoch is proportional to α^{-1}. Throughout early and intermediate times, whether or not the shell breaks out is determined by the product $\alpha\nu$, that is, on the momentum-loss rate of the wind. Finally, $\nu_{\rm crit}$ again rises at late times. In this case, the critical wind speed is independent of α and increases as $\tau^{1/2}$.

TABLE 1
CRITICAL WIND SPEED $\nu_{\rm CRIT}$

	α		
τ	1/3	1/10	1/30
0.25	4.19	12.7	37.1
0.50	5.90	17.9	52.0
1.00	7.67	23.1	67.0
2.00	7.34	21.0	59.8
4.00	4.48	11.6	32.2
8.00	2.81	5.80	16.1
16.0	2.89	3.33	8.06
32.0	3.71	3.87	4.18
64.0	5.10	5.16	5.29
128	7.14	7.18	7.23
256	10.1	10.1	10.1

Let us see in more detail how these results arise. The wind must combat the infall ram pressure and the gravitational force on the shell. At early times, we may neglect centrifugal distortion of the infall and consider only the spherically symmetric problem. In this case, the infall ram pressure at fixed radius varies as $\tau^{1/2}$ (recall eq. [39]). The gravitational force per unit shell mass rises as τ^1. To determine the force per area, we first note that the infall density ρ_i falls as $\tau^{-1/2}$, a consequence of the rising free-fall velocity. For a light wind, $\rho_w \ll \rho_i$, we may neglect the mass contribution of the wind. Since most of the mass of the shell is swept up, $\sigma \propto \rho_i \propto \tau^{-1/2}$ (see eqs. [62] and [64]), so the gravitational force per unit area on the shell $\sigma\mathscr{V}$ also behaves as $\tau^{1/2}$. Comparing the wind ram pressure (proportional to $\alpha\nu$) to the sum of infall ram pressure and gravity, we obtain $\nu_{\rm crit} \propto \tau^{1/2}/\alpha$.

The downturn in $\nu_{\rm crit}$ at $\tau \sim 1$ occurs because the star is now interior to the centrifugal radius. The decrease in the infall density along the z-axis relative to spherical accretion implies that breakout becomes easier. Because the shell's mass is dominated by the infall contribution, the decrease in the infall density along the axis decreases both the infall ram pressure and the gravitational force on the shell. At late times, the centrifugal radius has grown so large that the primary source of mass input to the shell is the wind. In this regime, the wind speed necessary for breakout is proportional to the stellar escape velocity, which in turn varies as $\tau^{1/2}$.

We compare these numerical results for $\nu_{\rm crit}$ with three analytical approximations in Figure 10. A hypothetical wind of speed $\nu = \nu_{\rm esc}$ (*diagonal dot-dashed line*) would be fast enough to break out if we neglect the mass and momentum fluxes to the shell from infall. We see that except for late times ($\tau \geq 10$), the wind must be considerably faster than the escape speed to drive a swept-up shell that will break out. At late times, our constant-speed wind can break out with $\nu < \nu_{\rm esc}$ because we have neglected gravitational deceleration of the preshock wind.[2] The second approximation is that of $\nu = \nu_{\rm ram}$, shown by the dashed line, yielding ram pressure balance of wind and infall at the stellar surface. This approximation underestimates the necessary wind speed for breakout by a factor of 1.9 at early times, when the infall is spherically symmetric, but it underestimates the critical speed by a much larger factor once the infall becomes significantly aspherical.

The two foregoing analytical approximations give a poor agreement with $\nu_{\rm crit}$ because the first neglects the infall ram

[2] Using modified wind conditions of such a coasting, decelerating wind of constant specific energy $e = V_w^2/2 - GM_*/r$ and numerically determining the corresponding critical speed for breakout with our code (Fig. 10, *filled triangles*), we see that the late-time critical curves are shifted vertically and converge to the escape speed. At early times, since breakout speeds were already much larger than the escape speed, the difference between a constant speed and a decelerating wind is negligible, and the critical curves are unchanged. Because no observed winds actually decelerate, we consider the constant-velocity curves to be more applicable.

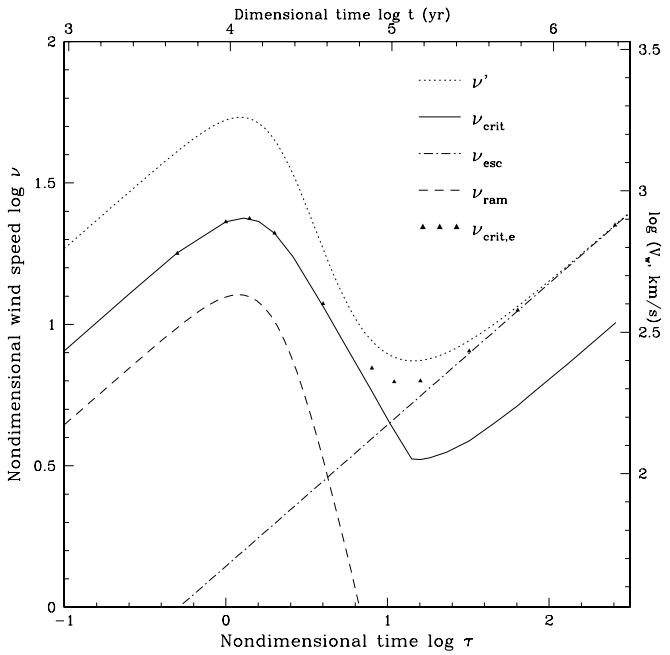

FIG. 10.—Minimum breakout wind speed vs. evolutionary time, compared with analytical arguments. All curves correspond to $\alpha = 0.1$. At bottom left (*dashed curve*) is the ram pressure balance condition at the launch point. At bottom right (*diagonal dot-dashed line*) is the condition of initial wind speed equal to the escape speed. The curve labeled $\nu_{\rm crit}$ gives numerical results for the critical wind speed. The top dotted curve gives the condition that the shocked shell initially moves at the escape speed. Filled triangles represent the critical condition for a decelerating wind (see text).

pressure, while the second neglects the gravitational force on the shell. To include in an analytic fashion the effect of both infall ram pressure and gravity on the shocked gas within the shell, we specify the condition that the initial *post-shock* gas be rising at the escape speed. According to equation (50), in order to have $u_{0,r} = V_{\rm esc}$, we obtain the necessary condition

$$\nu = \nu_{\rm esc}(1 + 2\eta^{1/2}) \ . \tag{71}$$

We cannot immediately apply this equation because $\eta = \rho_i/\rho_w$ itself depends on the wind speed. The density ratio is found from equations (64)–(66), where for $\theta = 0$ we have $f_r = -\sqrt{2}$ and $P_2(\cos\theta_0) = 1$, which yields

$$\eta = b^2 \frac{\nu}{\nu_{\rm esc}} \ , \tag{72}$$

where we have defined for brevity

$$b \equiv \frac{1}{\sqrt{\alpha(1 + 2\zeta_0)}} \ . \tag{73}$$

The solution ν' to equations (71) and (72) is found as the root of a quadratic equation, giving

$$\nu' = f\nu_{\rm esc}\left(b + \sqrt{b^2 + 1}\right)^2 \ , \tag{74}$$

which for $f = 1$ is the value of ν required to give the *post-shock, mixed* gas escape speed at the stellar surface. The ad hoc factor f allows us to consider the wind to be some fraction f of the speed required to give the shell escape speed at launch. The corresponding curve for $\alpha = 0.1$ and $f = 1$ is shown in Figure 10 (*dotted curve*). If we neglect changes in the infall momentum flux per unit solid angle once the shell is launched, ν' is expected to be an estimate of the necessary wind speed to launch a shell that will break out. In practice, as the shell advances, the forces on the shell change, and typically the wind weakens less quickly than the infall, so the above condition overestimates the required wind speed. Except for the vertical offset, however, the curve follows closely the shape of the numerically derived critical curve, suggesting $f \approx$ const throughout the evolution. By choosing $f = 0.45$, so as to fit the late-time behavior, an approximate fit to the critical curves is shown in Figure 9.

6.3. *Generalization to Anisotropic Wind*

The previously described calculations may be extended to anisotropic winds by defining angular dependences of the wind mass and momentum fluxes according to

$$\rho_w V_w = \frac{\dot{M}_w}{4\pi r^2} f_w(\theta) \ , \tag{75}$$

$$\rho_w V_w^2 = \frac{\dot{M}_w \bar{V}_w}{4\pi r^2} g_w(\theta) \ , \tag{76}$$

where $\bar{V}_w$ is the streamline-averaged wind speed and the functions f_w and g_w are normalized to have unit average value over 4π sr. Although a diversity of shell shapes may be generated in this fashion, we focus only on the behavior at the symmetry axis, where breakout is easiest. If the properties of the wind are smooth near the pole, i.e., $f_w'(0) = g_w'(0) = 0$, the shell has $R'(0) = 0$ and looks locally as though it is driven by an isotropic wind.

Figure 6 shows a numerical example. Here the dashed curves represent a shell driven by an anisotropic wind specifically chosen to have the same mass and momentum fluxes toward $\theta = 0$ as the isotropic wind (*solid curves*). We have chosen the asymmetric driving wind to have $\alpha = \frac{1}{6}$ and a density $\rho_w \propto f_w = g_w = \frac{1}{2}(1 + 3\cos^2\theta)$, with V_w independent of θ, while the values of ν and τ are unchanged from the spherical wind case. This angular dependence represents the lowest order expansion that is axisymmetric and of even parity and has been chosen arbitrarily to give a pole-to-equator density contrast of 4. Because the derived polar behavior $R_0(t)$ of a shell driven by an anisotropic wind follows that of a spherical wind having the same polar mass and momentum fluxes, the critical wind speed $\nu_{\rm crit}$ for breakout of an anisotropic wind may be determined from our numerical curves. Defining $\nu \equiv \bar{V}_w/V_*$, the equivalent spherical wind corresponds to $\alpha_{\rm sph} = \alpha f_w(0)$ and $\nu_{\rm sph} = \nu g_w(0)/f_w(0)$. A wind that is focused preferentially toward the poles mimics a spherical wind corresponding to a higher value of α and a reduced value of $\nu_{\rm crit}$, breaking out at an earlier time (see below). In our example, the $\alpha = \frac{1}{6}$ wind has $\alpha_{\rm sph} = \frac{1}{3}$ and the shell propagates along the axis like a bubble from an isotropic wind of higher α-value.

6.4. *The Breakout Time*

Given the curves for the critical wind speed for breakout (Fig. 9), we now wish to estimate the time at which breakout occurs. We first note that a wind whose speed is independent of τ would experience no trapped phase, since the curves for $\nu_{\rm crit}$ decrease as $\tau \to 0$. Although we are not offering a general theoretical account of protostellar winds, we note that a

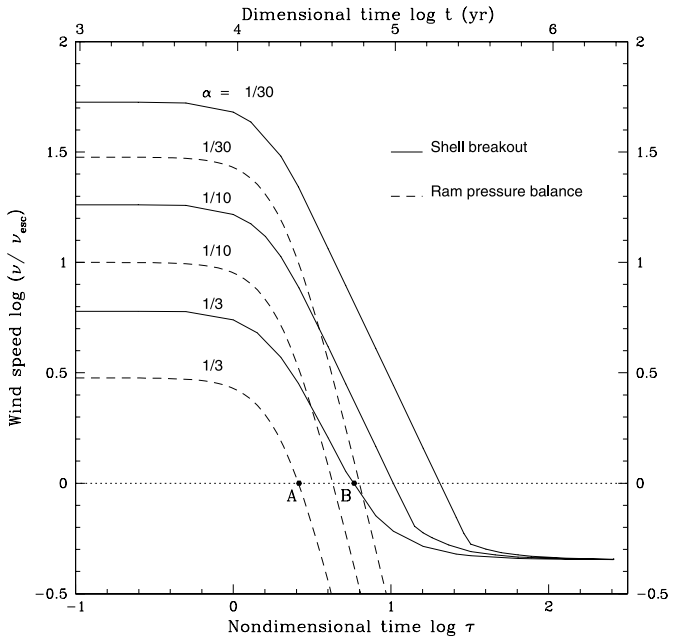

FIG. 11.—Critical wind speed for breakout (*solid curves*), in units of the free-fall (escape) speed, as a function of evolutionary time. The corresponding α-values are shown, as well as the wind speed necessary for ram pressure balance at the stellar surface (*dashed curves*). Assuming wind launch conditions $\nu_w/\nu_{\rm esc} = 1$ (i.e., following the horizontal line in this figure), evolution begins at the left edge of the plot with the wind unable to advance beyond the stellar surface until the line intersects the appropriate dashed curve. Then the trapped wind phase lasts until the line intersects the corresponding solid curve for breakout.

constant wind speed is unlikely on purely empirical grounds. Stars of all masses and ages tend to have V_w values roughly equal to the appropriate surface escape speed (Lamers & Cassinelli 1999). We therefore recast Figure 9 as a plot of $V_w/V_{\rm esc} = \nu/\nu_{\rm esc}$ versus τ (Fig. 11). For comparison, we have also plotted $\nu_{\rm ram}/\nu_{\rm esc}$, to delimit the end of the crushed wind phase, using equation (70) for $\nu_{\rm ram}$. Suppose, then, that $\nu/\nu_{\rm esc}$ were strictly a constant, equal to unity. Taking the case $\alpha = \frac{1}{3}$ in Figure 11, we see that the wind would first be able to advance from the stellar surface at $t \sim 25,000$ yr, but breakout would be achieved at $t \sim 54,000$ yr. For the $\alpha = 1/10$ model, these times increase to 41,000 and 98,000 yr, respectively. Our numbers rely on a relatively modest value of $\Omega_0 = 2 \times 10^{-14}$ s^{-1}. Based on equation (52), increasing Ω_0 by a factor of 2 would decrease the above breakout times by a factor of 0.63. Thus, the trapped outflow phase may be a significant fraction ($\sim$60%) of the time prior to breakout.

For the example we have shown, the breakout of the shell occurs at essentially all angles. However, this is not the case for all runs and is not true in general. Thus, our breakout time is to be interpreted as the time at which the wind first breaks out along the z-axis. At larger angles, the wind may be unable to break out until a later evolutionary time, resulting in simultaneous outflow and infall.

Usually, however, the wind escapes globally, as shown in Figures 5–7. The shell aspect ratio then begins and ends as unity, either at the stellar surface or far from the star. The maximum distortion, which is still modest, is attained at intermediate times, when the shell is a few AU from the stellar surface.

7. DISCUSSION

7.1. *Behavior during the Trapped Wind Phase*

Our recollapsing shells generally become unstable during the trapped wind phase. Portions that are initially inside neighboring regions fall faster, increasing any perturbation of an initially smooth surface. While our calculations do find this strong dynamical effect, we cannot detect the nonlinear instability of Vishniac (1994), which relies on a finite shell thickness. Our results make it clear, in any case, that the true behavior during the trapped wind phase is exceedingly complex. After a portion of the shell collapses to the stellar and disk surfaces, a new shock is immediately driven outward by the steady wind. Thus, there will simultaneously be contracting and expanding patches at different angles. Portions of the wind may escape temporarily between recollapsing fragments before falling back. While the details of this process cannot be followed by our computational method, we believe our calculated breakout times should still be reasonably accurate. In any event, this time cannot decrease by more than about a factor of 2, since the infall crushes the wind entirely at an earlier epoch.

One observational signature of the trapped wind phase would be fluctuations in luminosity due to the rising and recollapse of the shell. This luminosity arises from both the shocking of the wind and ambient gas. When a portion of the shell is rising, the corresponding wind component of luminosity decreases because of the lowered shock velocity. The infall component of the luminosity may either increase (because the shock velocity is raised) or decrease (because $|\boldsymbol{u}_i| = u_{\rm esc}$ decreases at larger radius). All luminosity fluctuations should increase in both period and amplitude with evolutionary time because as breakout is approached, the shell rises higher before recollapse. Further study is needed to determine the observed magnitude of these fluctuations, as well as the transport of radiation through the infalling gas.

As indicated earlier, the wind may also break out along the axis, while portions of the shell at larger angles continue oscillatory behavior. In this case, one would observe a bipolar jet accompanied by quasi-periodic fluctuations in luminosity.

7.2. *Comments on Collimation*

Figures 5–7 show that the lobelike appearance of our shells is a transient phenomenon created by anisotropy in the infalling gas. In particular, this elongated morphology cannot be identified with the collimation seen in Herbig-Haro jets. Our assumed mixing of shocked wind and infall is, in fact, an agent for *decollimation*. A fluid element of the wind, initially moving radially outward, acquires a positive θ-velocity. Thus, there is a tendency for gas to move toward the disk plane, despite the (temporary) elongation of the shell.

Our mixing assumption was made purely for computational simplicity. In reality, there must be considerable shear between the two shocks. This shear may have several important consequences. First, shocked wind may be refracted along the shell's inner surface toward the polar axis, resulting in a more jetlike flow. Such a geometry would resemble the early outflow model of Cantó (1980), although the latter pictured a shell in pressure balance with a static, external medium. A second effect is that shocked, ambient gas will

move tangentially toward the *equator*. The overall result will be a shell of lower mass that is less confined by stellar gravity. The duration of the trapped wind phase will therefore be reduced, resulting in earlier breakout. However, we note that even in the limit of no mixing, the wind must still be crushed by infall at a sufficiently early epoch. In future calculations, we hope to explore quantitatively the consequences of relaxing the mixing assumption.

In a series of numerical simulations carried out through the 1990s, A. Frank and colleagues found that the interaction of a spherical wind and infall produces very strong collimation. However, these studies (beginning with Frank & Noriega-Crespo 1994) modified the equations for infall, thus obtaining a much larger density anisotropy than adopted here. For example, Frank & Mellema (1996) used an equator-to-pole density contrast of 50–70, while Delamarter, Frank, & Hartmann (2000) allow this ratio to exceed 10^3. For comparison, the density contrast in our outflow exceeds 50 only for $0.96 \lesssim R/R_{\rm cen} \lesssim 1.08$. Our escaping shell spends relatively little time within this region, sweeping up a small amount of mass. We conclude that a spherical or modestly anisotropic wind undergoes little collimation through interaction with a physically realistic infall, unless it is through the shear effect described above.

Our finding of an early, trapped wind phase is a similarly robust result, although it was missed in previous simulations. Frank & Mellema (1996) adopt such a large wind velocity ($V_w \geq 500$ km s^{-1}) that the infall ram pressure is overwhelmed. Mellema & Frank (1997) did find oscillating shells that, under some conditions, collapsed. However, the driver of their oscillations was a variable wind, so that collapse always coincided with the weakest outflow phase. More recently, Delamarter et al. (2000) utilized as an infalling background the flattened, rotating cloud of Hartmann, Calvet, & Boss (1996). Although they claim that especially weak winds may be stifled entirely by infall, their numerical results always show the wind escaping through at least a narrow solid angle through the symmetry axis.

We maintain, based on the arguments presented above, that early wind crushing and eventual breakout are inescapable features within a realistic account of the wind-infall interaction. In contrast, a strong, untrapped wind that is present ab initio, as in previous simulations, would have already modified substantially the background infall, rendering subsequent results of dubious validity. Our own calculations of breakout can provide useful starting conditions for future investigators who wish to follow the wind evolution well beyond this critical, early phase.

7.3. *Further Observational Considerations*

We have seen that, for canonical values of our parameters, the wind is trapped for a period of roughly 50,000 yr. Although the evolutionary status of the most embedded sources is by no means secure, those designated as Class 0 (André et al. 1993) are generally considered to be the youngest. They are detectable only at far-infrared and submillimeter wavelengths and have spectral energy distributions corresponding to dust temperatures of roughly 30 K. An additional argument for their extreme youth is their relatively low population. In a submillimeter survey of ρ Ophiuchi, Motte, André, & Neri (1998) found that Class I sources outnumber those of Class 0 by a factor of 10. Since the former have traditionally been assigned ages of order 10^5 yr (Kenyon et al. 1990), Class 0 stars could be as young as 10^4 yr, if the population is forming in steady state fashion. Visser, Richer, & Chandler (2002), in their recent SCUBA survey of Lynds dark clouds, have challenged these figures. They find nearly equal numbers of Class 0 and I sources and conclude that the former also have ages of roughly 10^5 yr.

Regardless of the outcome of this controversy, both surveys, as well as other studies, have found that essentially all stars with massive, dusty envelopes produce winds, as evidenced by associated CO outflows. Where, then, is the trapped phase? We see two possible answers to this question. The first, and less likely, is that our choice of input parameters requires adjustment. However, the necessary changes would be severe. For fixed α, ν, and τ, $t_{\rm break}$ scales as $R_*^{1/3} a_0^{-1/3} \Omega^{-2/3}$. It strains credibility to suppose, for example, that the cloud sonic speed a_0 is so high that $t_{\rm break}$ is reduced by an order of magnitude. In addition to this change of scale, we may change nondimensional solutions, by assuming a faster wind (greater ν). As seen in Figure 11, the breakout time is relatively insensitive to ν until a value is reached where the trapped wind disappears entirely (where the dashed curves are horizontal). This option, however, would imply very high wind speeds ($V_w \sim 3 V_{\rm esc}$ for $\alpha = \frac{1}{3}$, or $V_w \sim 10 V_{\rm esc}$ for $\alpha = 1/10$). As noted in § 6.3, making the wind more anisotropic effectively raises α and also leads to earlier breakout. Winds launched via the magnetocentrifugal mechanism, however, typically have modest anisotropy until they propagate a considerable distance (see, e.g., Najita & Shu 1994).

A second, and more plausible, answer is that we are *already* witnessing at least partially trapped winds. Following the arguments in § 7.1, it may be that simultaneous infall and outflow occur well before our idealized model indicates the onset of breakout. It would be extremely interesting, in this regard, to monitor the temporal variability of outflows from Class 0 sources.

8. CONCLUSIONS

We have presented a detailed numerical calculation of the interaction between a spherical, protostellar wind and an anisotropic, infalling envelope. The anisotropy in our model is derived from the rotation of the star's parent cloud core. Collapse is assumed to proceed in inside-out fashon from a singular, isothermal sphere, in the absence of magnetic forces. We have idealized the double-shock interaction region as a thin shell that is well mixed internally. After demonstrating that our previous, quasi-steady solutions are dynamically unstable, we have followed the shell dynamics in a fully time-dependent manner.

At very early times, the wind is crushed by ram pressure associated with infalling matter. Wind breakout is delayed by the gravitational force exerted on the shocked material. The shell must not only be supported by wind ram pressure but must have sufficient kinetic energy to escape the star's potential well, even while gathering additional mass from the envelope. Breakout would occur earlier if either the wind or infall were more anisotropic, or if we were to include the internal shear between the shock surfaces.

Bearing in mind the observations of jets and outflows from embedded stars, we acknowledge two important limitations of our model. First, our assumption of complete, early trapping may be incorrect because of shell fragmentation. Second, the observed collimation of stellar jets over

long distances is not approached asymptotically in our calculation. Instead, our shells, while they are temporarily elongated, eventually become spherical. Jet collimation may be a consequence of magnetic pinching in the wind itself or of a cloud background that is very different from the one we assume here. An initially more anisotropic cloud core will, of course, yield an altered pattern of infall. Alternatively, a shallower falloff in the background density will give rise to crossing shocks in the interaction region (see, e.g., Cantó, Raga, & Binette 1989). These shocks further aid in wind collimation.

F. P. W. acknowledges helpful discussion with S. Lizano and is grateful to the NSF International Researchers Fellowship Program and CONACyT/México for financial support. Part of the calculations were performed at the Observatoire de la Côte d'Azur as a Henri Poincaré Fellow. S. W. S. was supported by NSF grant AST 99-87266.

REFERENCES

André, P., Ward-Thompson, D., & Barsony, M. 1993, ApJ, 406, 122
Bandiera, R. 1993, A&A, 276, 648
Barranco, J. A., & Goodman, A. A. 1998, ApJ, 504, 207
Blandford, R. D., Begelman, M. C., & Rees, M. J. 1984, Rev. Mod. Phys., 56, 255
Blondin, J. M., & Koerwer, J. F. 1998, NewA, 3, 571
Cantó, J. 1980, A&A, 86, 327
Cantó, J., Raga, A. C., & Binette, L. 1989, Rev. Mexicana Astron. Astrofis., 17, 65
Cassen, P., & Moosman, A. 1981, Icarus, 48, 353
Cho, J., Lazarian, A., & Vishniac, E. T. 2002, ApJ, 566, L49
Delamarter, G., Frank, A., & Hartmann, L. 2000, ApJ, 530, 923
Dgani, R., Van Buren, D., & Noriega-Crespo, A. 1996, ApJ, 461, 927
Frank, A., & Mellema, G. 1996, ApJ, 472, 684
Frank, A., & Noriega-Crespo, A. 1994, A&A, 290, 643
Giuliani, J. L. 1982, ApJ, 256, 624
Hartmann, L., Calvet, N., & Boss, A. 1996, ApJ, 464, 387
Jijina, J., Myers, P. C., & Adams, F. C. 1999, ApJS, 125, 161
Kenyon, S. J., Hartmann, L. W., Strom, K. M., & Strom, S. E. 1990, AJ, 99, 869
Lamers, J. G. L. M., & Cassinelli, J. P. 1999, Introduction to Stellar Winds (Cambridge: Cambridge Univ. Press)
Li, Z., & McKee, C. F. 1996, ApJ, 464, 373
Mac Low, M.-M., & McCray, R. 1988, ApJ, 324, 776
Mellema, G., & Frank, A. 1997, MNRAS, 292, 795
Motte, F., André, P., & Neri, R. 1998, A&A, 336, 150
Najita, J., & Shu, F. H. 1994, ApJ, 429, 808
Raga, A. C., Noriega-Crespo, A., Cantó, J., Steffen, W., van Buren, D., Mellema, G., & Lundqvist, P. 1997, Rev. Mexicana Astron. Astrofis., 33, 79
Shu, F. H. 1977, ApJ, 214, 488
Shu, F. H., Adams, F. C., & Lizano, S. 1987, ARA&A, 25, 23
Shu, F. H., Lada, C., Ruden, S. V., & Lizano, S. 1991, ApJ, 370, L31
Stahler, S. W. 1988, ApJ, 332, 804
Stahler, S. W., Korycansky, D. G., Brothers, M. J., & Touma, J. 1994, ApJ, 431, 341
Terebey, S., Shu, F. H., & Cassen, P. 1984, ApJ, 286, 529
Vazquez-Semadeni, E., Ballesteros-Paredes, J., & Klessen, R. K. 2003, ApJ, 585, L131
Vishniac, E. T. 1994, ApJ, 428, 186
Visser, A. E., Richer, J. S., & Chandler, C. J. 2002, AJ, 124, 2756
Wilkin, F. P. 1996, ApJ, 459, L31
Wilkin, F. P., & Stahler, S. W. 1998, ApJ, 502, 661 (Paper I)